# Near-Field Power Density Mapping of Close-to-Body Low-Power mmWave Devices

Massinissa Ziane, Artem Boriskin, Maxim Zhadobov

# Near-field Power Density Mapping of Close-to-body Low-power mmWave Devices

Massinissa Ziane, Artem Boriskin, *Senior Member, IEEE,* and Maxim Zhadobov, *Senior Member, IEEE*

***Abstract*—This letter introduces a method for power density (PD) measurement of low-power millimeter-wave (mmWave) devices, accounting for antenna/body coupling. This technique employs a thin solid absorbing structure with equivalent scattering properties used to convert the absorbed power into a heat pattern measured by an infrared (IR) camera. The measured IR pattern is then used to reconstruct the PD distribution. The lock-in technique is used to enhance the signal-to-noise ratio (SNR). It consists in filtering the ambient IR noise as well as removing the parasitic heat conduction effect. The reduction of noise enables achieving a measurement sensitivity of the order of 1 mW/cm$^2$, substantially overcoming the sensitivity without lock-in ($>$ 10 dB). The proposed approach is experimentally validated for a conical horn antenna at 60 GHz. For the first time, this study demonstrates the sensitivity of IR-based measurements sufficient enough to assess the compliance of medium- and low-power wireless devices above 6 GHz.**

***Index Terms*—Absorbed power density (APD), dosimetry, millimeter-wave measurements, phantoms.**

## I. Introduction

THE increasing need for high data rates, reliable wireless connection and improved latency is resulting in continuous shifting of operating frequencies towards millimeter waves (mmWaves) [1], [2]. This band is foreseen for numerous applications such as 5G/xG, telemedicine, remote driving, IoT, smart industry and augmented reality [3-5]. Near-field measurements in free space or in operating environments (e.g. smartphone close to body) represent an essential step in design as well as in performance and compliance testing of wireless devices [6], [7].

Infrared (IR) imaging allows for non-perturbing, isotropic, and broadband 2D measurement of the electromagnetic (EM) power distribution with sub-mm resolution, in the far [8] as well as in the near field [9]–[15]. To this end, an absorbing dielectric structure is used to convert the EM energy into heat. The temperature rise on its surface generates an IR signal remotely recorded by an IR sensor. The EM power distribution is consequently retrieved by post-processing from the measured IR signal. This method is particularly suitable for power density (PD) measurement at mmWaves due to increasing with frequency losses resulting in a more effective conversion of the EM energy to heat.

Accurate and realistic user exposure assessment requires accounting for the impact of the presence of user on a wireless device under test and PD due to the antenna/body interactions. It was demonstrated that ignoring antenna/body coupling may result in a significant (up to a factor of two) underestimation of the absorbed PD [16]. A technique for PD measurement accounting for antenna/body interactions at mmWaves was reported in [17]. This technique employs a thin solid absorbing structure reproducing the scattering characteristics of human skin. In that study, a high input power (several hundreds of mW, corresponding to an incident PD (IPD) of hundreds of mW/cm$^2$) was required for reliable measurements due to a high level of environmental IR noise. This parasitic noise results in a poor signal-to-noise ratio (SNR), limiting so far application of this technique to characterization of high-power wireless devices.

In this letter, we introduce a novel approach for IR-based measurement of PD with reduced noise resulting in enhanced SNR and sensitivity. Limited sensitivity is the major bottleneck preventing the use of IR imaging for dosimetry and over-the-air (OTA) characterization of medium- and low-power wireless devices (such as smartphones, tablets, etc.). Improved sensitivity achieved in this study enables, for the first time, IR-based characterization of medium- and low-power close-to-body mmWave devices with the total radiated power (TRP) down to mW.

The paper is organized as follows. Section II introduces the measurement setup as well as its key building block – solid thin dielectric structure (referred hereafter as phantom) – designed to reproduce the scattering characteristics of the human skin and acting as mmWave to IR converter. Section III presents the signal processing technique (lock-in) used to suppress the noise level through spectral filtering. In Section IV, the proposed approach is experimentally validated at 60 GHz. Finally, conclusions are drawn in Section V.

## II. Measurement System

### A. Experimental Setup

The experimental setup is illustrated in Fig. 1. The antenna under test (AUT) is located at distance $d$ from the surface S1 of the phantom (described in detail in Section II.B). A narrowband mmWave power generator (QuinStar, CA, USA)

Manuscript submitted May 03, 2023.

This work was supported by the French National Research Program for Environmental and Occupational Health of ANSES (2018/2 RF/07) through NEAR 5G project and by Labex CominLabs (ANR-10-LABX-07-01) through EM-ART project. It was also partly supported by "Région Bretagne" (ARED program) and by the French Ministry of Higher Education and Research (MESR); by Brittany Region, Ministry of Higher Education and Research, Rennes Métropole and Conseil Départemental, through the CPER Project SOPHIE/STIC and Ondes; by French National Center for Scientific Research (CNRS).

M. Ziane, A. Boriskin, and M. Zhadobov are with Univ Rennes, CNRS, IETR (Institut d'Électronique et des Technologies du numéRique), UMR 6164, 35000, Rennes, France (email: maxim.zhadobov@univ-rennes.fr).

Color versions of one or more of the figures in this article are available online at http://ieeexplore.ieee.org

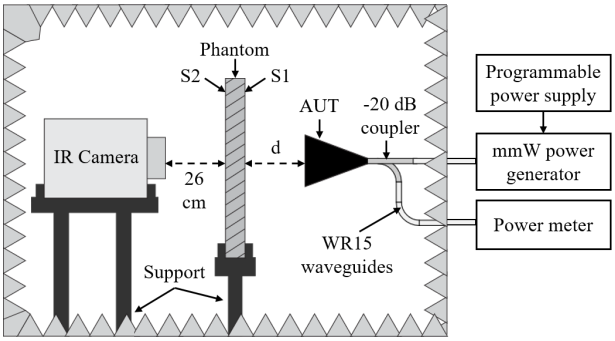


Fig. 1. Conceptual view of the measurement setup.

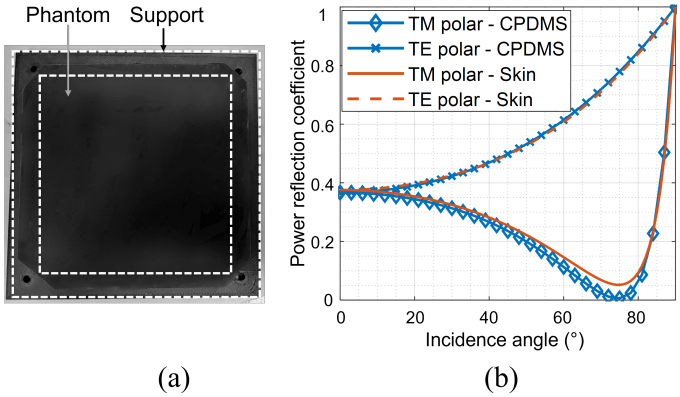


Fig. 2. Phantom: (a) fabricated prototype, (b) power reflection coefficient for parallel (TM) and perpendicular (TE) polarizations at 60 GHz.

is used to feed the AUT at 60 GHz through a set of WR15 rectangular waveguides. The waveform and frequency of the input signal are controlled using a programmable power supply (HMP 4040, Rohde and Schwarz, Munich, Germany). The input power level is measured through a -20 dB coupler (V752D, Hewlett Packard, CA, USA) using a power meter (E4418B, Agilent, CA, USA). As a validation example, we used a V-band (50-75 GHz) linearly-polarized conical horn antenna with 21.4 dBi gain.

The heat pattern at the surface S2 of the phantom is recorded by an IR camera (SC5600, FLIR Systems, OR, USA) located 26 cm from the phantom. The camera operates in the 3.5–5 $\mu$m range with the spatial resolution of 640×512 pixels (for the selected distance, the pixel size is 0.14 mm).

### B. Phantom

The thin solid absorbing structure used for conversion of the mmWave power to heat was designed following the approach detailed in [17]. The phantom is optimized to reproduce the reflection coefficient of the human skin and therefore to perturb the AUT in the same way as it would be perturbed by the presence of a human body. To this end, the thickness (1.8 mm) and the complex permittivity ($\epsilon_r = 12.5 - 3.625j$ at 60 GHz) are jointly chosen to provide the desired performance. The selected thickness results in a higher temperature rise compared to bulk phantoms thus contributing to enhancement of SNR. Note that, even if for such phantom the complex permittivity of the phantom is different from the one of skin, the PD at the phantom/air interface (S1) is the same as the one at the skin/air interface due to the energy conservation principle.

The spatial-temporal heat pattern remotely recorded by the IR camera at S2 is converted to the PD at S1 following the post-processing procedure detailed in [18]. The phantom structure enables obtaining similar heat distributions at S1 and S2, thus facilitating the PD retrieval simultaneously decreasing the reconstruction error. Note that the PD retrieval procedure does not require all incident EM power to be absorbed in the phantom (here roughly 95 % of power transmitted through the upper surface is absorbed in the phantom). However, the power dissipation in the phantom should be high enough to obtain a measurable temperature rise.

The phantom structure is fabricated using carbon black powder (40 %) and PDMS (Fig. 2(a)) following the process detailed in [19]. The phantom is attached to a hollow rectangular frame made of acrylonitrile butadiene styrene (ABS). The power reflection coefficient of the fabricated prototype compared to that of human skin is shown in Fig. 2(b). It is equal to 36.7 % for the normal incidence (0.9 % deviation compared to the Gabriel's dry skin model [20]). The maximum difference of 4.6 % found for TM polarization at the pseudo-Brewster angle of 75° is attributed to the difference in the imaginary part of carbon-PDMS ($\epsilon_r^{''} = 3.63$) compared to skin ($\epsilon_r^{''} = 11.9$). Note that for most of practical applications, the angular range of interest is limited to 45° in respect to the normal incidence. Therefore, the mismatch around the Brewster angle is expected to have a negligible effect.

The thermal conductivity $k = 0.48$ W·m$^{-1}$·K$^{-1}$ and specific heat capacity $c = 1259$ J· Kg$^{-1}$·K$^{-1}$ were measured using guarded hot disk and differential scanning calorimetry methods, respectively. The hemispherical spectral normal emissivity ($\epsilon_{\lambda,N}$) is equal 0.94 (measured using an IR spectrometer at 20 °C in the 3.5–5 $\mu$m range). The convective heat transfer coefficient $h$ of the phantom was set to 5 W·m$^{-2}$·°C$^{-1}$ [21].

## III. Noise Reduction

Enhancement of sensitivity and SNR in IR-based PD measurements is crucial for enabling characterization of low-power mmWave signals. One way to achieve this is to reduce the noise level of the measured IR signal by means of spectral filtering using the lock-in method. In this method, the amplitude of the AUT input power is modulated by a periodic waveform in order to: 1) remove the ambient noise, thus increasing the SNR, 2) mitigate the heat conduction effect, thus increasing correlation between the heat pattern and mmWave PD distribution. The steady-state lock-in implemented in this study is detailed hereafter.

### A. Periodic Excitation

The signal $S(t)$ is used to modulate the input power (square-wave on/off modulation) at frequency $f_{lock} = 1/T_{lock}$ (Fig. 3(a)):

$$S(t) = \frac{1}{2}A(1 + F_{sw}(T_{lock}, t)), \quad (1)$$

where $A$ is the peak-to-peak amplitude and $F_{sw}(T_{lock}, t)$ is the square-wave function. $S(t)$ can be analytically expressed as the sum of low-frequency (LF) and high-frequency (HF) signal components (Fig. 3(b) and Fig. 3(c), respectively):

$$S(t) = S_{LF} + S_{HF}(t), \tag{2}$$

with $S_{LF} = \frac{1}{2}A$ and $S_{HF}(t) = \frac{1}{2}A \cdot F_{sw}(T_{lock}, t)$.

### B. Steady-state Heat Dynamics

Absorbed by the phantom mmWave power induces temperature rise $T(t)$ (Fig. 4(a)). $T(t)$ is defined as the sum of low-frequency and high-frequency thermal components associated with $S_{LF}$ and $S_{HF}(t)$, respectively. Accounting for the environmental ambient noise, described by Gaussian white noise $N(t)$, the total induced temperature rise $T(t)$ can be expressed as:

$$T(t) = T_{LF}(t) + T_{HF}(t) + N(t), \tag{3}$$

where $T_{LF}(t)$ is the low-frequency time-average temperature increase and $T_{HF}(t)$ is the high-frequency oscillating part of $T(t)$.

$T(t)$ is measured at steady state, where $T_{HF}(t)$ and $T_{LF}(t)$ are expressed as:

$$T_{HF}(t) = \Delta T_0 \cdot F_{tw}(T_{lock}, t), \tag{4}$$

and:

$$T_{LF}(t) = T_{ss}, \tag{5}$$

where $\Delta T_0$ is the peak-to-peak amplitude of temperature oscillations at steady-state, $F_{tw}(T_{lock}, t)$ is the oscillation function schematically represented by a triangular-wave function in Fig. 4(a), and $T_{ss}$ is the mean steady-state temperature. Under experimental conditions of this study, the steady state is reached after roughly $t_0 = 5$ min of exposure.

### C. Frequency of Amplitude Modulation

$\Delta T_0$ represents the temperature rise (peak-to-peak amplitude of $T_{HF}(t)$) during $T_{lock}/2$ (Fig. 4(a)). The PD is directly proportional to $\Delta T_0$. However, this is valid only for sufficiently short $T_{lock}$. Indeed, increasing $T_{lock}$ would result in the parasitic heat conduction effect. On the other hand, reducing $T_{lock}$ would decrease the useful signal $\Delta T_0$. The optimal tradeoff between 1) minimizing the heat conduction effect and hence maximizing the correlation between PD and $\Delta T_0$ ($> 98\%$) and 2) enhancing the useful signal amplitude guaranteeing a sufficient IR image contrast (>10 dB) is found for $T_{lock} = 5$ s ($f_{lock} = 0.2$ Hz). This tradeoff is derived for the phantom employed in this study and AUT with a peak IPD = 22 mW/cm$^2$.

### D. Noise Filtering

$\Delta T_0$ is de-embedded from $T(t)$ by filtering $T_{LF}(t)$ and $N(t)$ in (3). This is performed using the following steps:

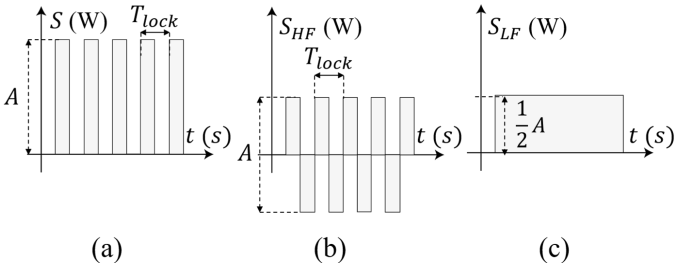


Fig. 3. Modulation signal: (a) $S(t)$, (b) $S_{HF}(t)$, (c) $S_{LF}$.

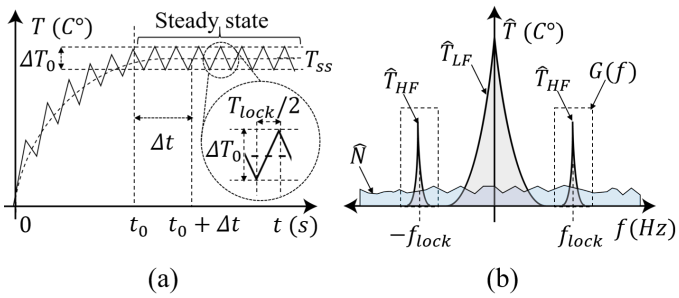


Fig. 4. Temperature dynamics: (a) time domain, (b) frequency domain (steady-state).

*1)* **Discrete Time Fourier Transformation:** $T(t)$ is a discrete function ($T(n)$ with $t = n/f_s$, where $f_s$ is the sampling frequency) recorded at the time interval $[t_0; t_0 + \Delta t]$. The discrete time Fourier transformation (DTFT) is applied to convert $T(n)$ to the frequency domain ($\hat{T}$):

$$\hat{T}(f) = \sum_{n=-\infty}^{+\infty} T(n) e^{-j2\pi fn}. \tag{6}$$

Fourier transformation is a linear mathematical operation, hence, using (3) in (6) yields:

$$\hat{T}(f) = \hat{T}_{LF}(f) + \hat{T}_{HF}(f) + \hat{N}, \tag{7}$$

where $\hat{T}_{LF}$, $\hat{T}_{HF}$, and $\hat{N}$ are the spectra of $T_{LF}$, $T_{HF}$, and $N$, respectively, schematically represented in Fig. 4(b).

*2)* **Spectral Filtering and Inverse Fourier Transformation:** Band-pass filtering at $f_{lock}$ allows to remove $\hat{T}_{LF}$ and $\hat{N}$:

$$\hat{T}_{HF}(f) = \hat{T}(f) \cdot G(f), \tag{8}$$

with $G(f) = 0$ for $f \neq f_{lock}$ and $G(f) = 1$ for $f = f_{lock}$. The inverse DTFT of $\hat{T}_{HF}$ is applied to retrieve $T_{HF}$ and consequently $\Delta T_0$:

$$T_{HF}(n) = \int_{2\pi} \hat{T}_{HF}(f) e^{j2\pi fn}. \tag{9}$$

A part of $\hat{N}$ at $f_{lock}$, which cannot be filtered, is mitigated by maximizing $\Delta t$ and $f_s$. To this end, we used $\Delta t = 180$ s, $f_s = 50$ Hz.

## IV. Experimental Validation

As a validation example, measurements are performed for a conical horn antenna for $A = 36$ mW at $d = 3.5$ mm (Fig. 5). In this configuration, the peak IPD equals to 22 mW/cm$^2$. The

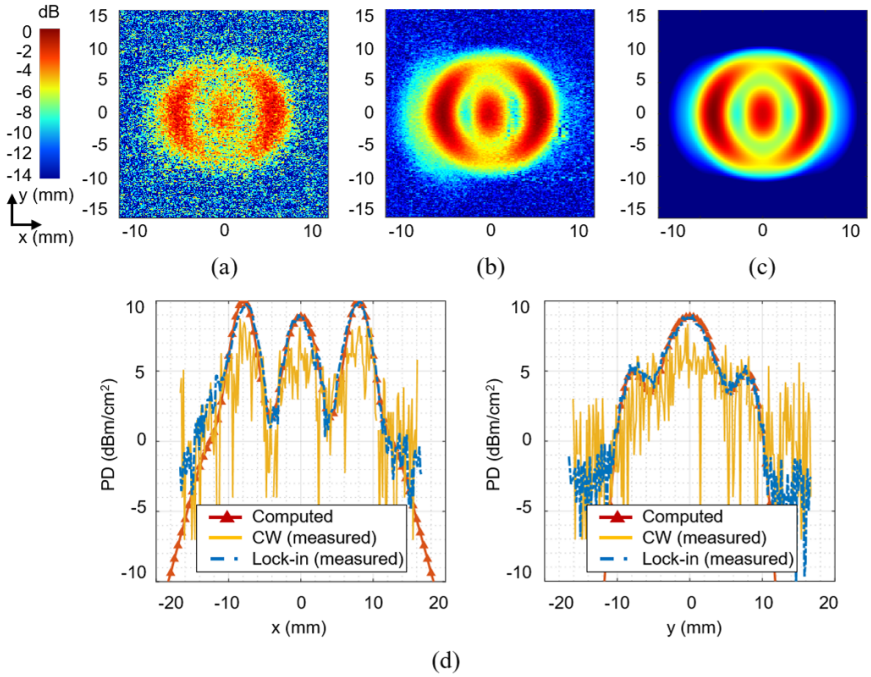


Fig. 5. PD distributions for the conical horn antenna at $d = 3.5$ mm: (a) measured using non-periodic CW excitation, (b) measured applying lock-in, and (c) simulated. (d) 1D PD profiles along x-axis ($y = 0$ mm) (left) and y-axis ($x = 0$ mm) (right) (absolute values are provided for the numerical data and measurement results are normalized to the peak value).

distance $d = 3.5$ mm corresponds to a near-field PD pattern with multiple lobes, requiring higher measurement accuracy compared to a far-field configuration where the PD distribution has only one main lobe (e.g. Gaussian-like distribution).

The PD distribution obtained using a non-modulated 36 mW continuous-wave (CW) excitation after 2.5 s = $T_{lock}/2$ of exposure is shown in Fig. 5(a). Results obtained using lock-in demonstrate substantial improvement of the image quality and sensitivity (Fig. 5(b)). The measured PD distributions are compared to PD computed using the finite integration technique (FIT) implemented in CST Microwave Studio (Figs. 5(c,d)).

The PD distributions are compared using a correlation coefficient $\Upsilon$ indicating how closely the two relative distributions fit [22]:

$$\Upsilon = \frac{\sum_m \sum_n (X_{mn} - \bar{X})(Y_{mn} - \bar{Y})}{\sqrt{\sum_m \sum_n (X_{mn} - \bar{X})^2 \sum_m \sum_n (Y_{mn} - \bar{Y})^2}}, \quad (10)$$

where $X$ and $Y$ are the distributions to compare, $\bar{X}$ and $\bar{Y}$ are respectively the mean values of $X$ and $Y$.

The results demonstrate a very good agreement between the PD distributions measured applying lock-in (and SNR $\approx$ 11 dB) and the simulated one ($\Upsilon = 98.7$ %). The proposed technique demonstrates more than 10 dB gain compared to the CW excitation (SNR $\approx$ 1 dB). Note that a higher SNR can be obtained for a CW signal with a longer duration (e.g. 5.3 dB for 20 s), however the enhanced heat conduction will lead to lower correlation between the measured heat pattern and PD ($\Upsilon = 81.9$ %).

The sensitivity of the method can be defined as the PD level that can be reliably measured using the proposed technique. Fig. 5(d) (blue curve) demonstrates the sensitivity of about 1 mW/cm$^2$, achieved thanks to the noise reduction through lock-in. This represents a significant improvement compared to conventional IR-based measurements [17], with the sensitivity of the order of 10 mW/cm$^2$ limited by the level of the ambient noise (Fig. 5(d) – yellow curve).

The enhanced sensitivity of the proposed technique makes it promising for dosimetry and compliance testing. According to [23], the main dosimetry quantity above 6 GHz is the absorbed power density (APD) defined as PD averaged over 4 cm$^2$ or 1 cm$^2$. Thus APD can be calculated by spatial averaging of PD retrieved from high-resolution IR measurements.

## V. Conclusion

In this study, we introduced a novel approach for high-resolution near-field mapping of PD based on IR imaging applied to characterization of low-power mmWave devices accounting for antenna/body interaction. Enhanced sensitivity is achieved by post-processing the measured signal using lock-in. The proposed technique is validated at 60 GHz for conical horn antenna. An excellent agreement is found between simulated and measured PD using lock-in (correlation $>$ 98 %). The results show that the IR-based technique can be used for reliable PD measurement at the IPD levels as low as 1 mW/cm$^2$ (corresponding to sensitivity improvement at least by a factor of 10 compared to conventional IR-based measurements using CW excitation [17]). For the first time, this study demonstrated the sensitivity of IR-based measurements sufficient enough to assess the compliance of medium- and low-power wireless devices above 6 GHz.

## REFERENCES


[1] T. S. Rappaport and al., "Millimeter wave mobile communications for 5G cellular: It will work!," *IEEE Access*, vol. 1, pp. 335-349, May 2013, doi: 10.1109/ACCESS.2013.2260813.

[2] "High five," *Nat. Electron.*, vol. 3, no. 1, p. 1, Jan. 2020, doi: 10.1038/s41928-020-0368-1.

[3] H. Yin, L. Zhang, and S. Roy, "Multiplexing URLLC traffic within eMBB services in 5G NR: Fair scheduling," *IEEE Trans. Commun.*, vol. 69, no. 2, pp. 1080-1093, Feb. 2021, doi: 10.1109/TCOMM.2020.3035582.

[4] Q. Qi, X. Chen, C. Zhong, and Z. Zhang, "Integrated sensing, computation and communication in B5G cellular internet of things," *IEEE Trans. Wirel. Commun.*, vol. 20, no. 1, pp. 332-344, Jan. 2021, doi: 10.1109/TWC.2020.3024787.

[5] R. Liu, G. Yu, J. Yuan, and G. Y. Li, "Resource management for millimeter-wave ultra-reliable and low-latency communications," *IEEE Trans. Commun.*, vol. 69, no. 2, pp. 1094-1108, Feb. 2021, doi: 10.1109/TCOMM.2020.3036046.

[6] *Assessment of Power Density of Human Exposure to Radio Frequency Fields from Wireless Devices in Close Proximity to the Head and Body (Frequency Range of 6 GHz to 300 GHz)*, IEC/IEEE 63195-2, May 2022.

[7] *Measurement Procedure for the Assessment of Specific Absorption Rate of Human Exposure to Radio Frequency Fields from Hand-held and Body-worn Wireless Communication Devices - Human Models, Instrumentation and Procedures (Frequency Range of 4 MHz to 10 GHz)*, IEC/IEEE 62209-1528, Oct. 2020.

[8] P. Levesque, P. Brémond, J.-L. Lasserre, A. Paupert, and D. L. Balageas, "Performance of FPA IR cameras and of their improvement by time, space and frequency data processing: Part II - Application to the thermographic measurement of microwave fields," *Quant. InfraRed Thermogr. J.*, vol. 2, no. 2, pp. 237-250, Dec. 2005, doi: 10.3166/qirt.2.237-250.

[9] N. Ribiere-Tharaud, M. Lambert, and P. Levesque, "Wideband validation of a phase retrieval process applied to infrared planar near-field measurements," *Prog. Electromagn. Res. B*, vol. 23, pp. 39-54, Jul. 2010, doi: 10.2528/PIERB10040906.

[10] N. Chahat, M. Zhadobov, L. Le Coq, S. I. Alekseev, and R. Sauleau, "Characterization of the interactions between a 60-GHz antenna and the human body in an off-body scenario," *IEEE Trans. Antennas Propag.*, vol. 60, no. 12, pp. 5958-5965, Dec. 2012, doi: 10.1109/TAP.2012.2211326.

[11] A. K. Fall, P. Besnier, C. Lemoine, M. Zhadobov, and R. Sauleau, "Experimental dosimetry in a mode-stirred reverberation chamber in the 60-GHz band," *IEEE Trans. Electromagn. Compat.*, vol. 58, no. 4, pp. 981-992, Aug. 2016, doi: 10.1109/TEMC.2016.2550803.

[12] C. Leduc and M. Zhadobov, "Impact of antenna topology and feeding technique on coupling with human body: Application to 60-GHz antenna arrays," *IEEE Trans. Antennas Propag.*, vol. 65, no. 12, pp. 6779-6787, Dec. 2017, doi: 10.1109/TAP.2017.2700879.

[13] M. Zhadobov, C. Leduc, A. Guraliuc, N. Chahat, R. Sauleau, "Antenna/human body interactions in the 60 GHz band: State of knowledge and recent advances," in *Advances in Body-centric Wireless Communication: Applications and State-of-the-art*, UK: The IET, 2016, ch. 5, pp. 97-142.

[14] T. Crepin, F. Issac, D. Prost, and S. Bolioli, "Microwave electric field imaging of metamaterials using thermoemissive films," *IEEE Antennas Propag. Mag.*, vol. 56, no. 3, pp. 37-42, Jun. 2014, doi: 10.1109/MAP.2014.6867681.

[15] D. Prost, "Measurement of the amplitude and polarization of the electric field by electromagnetic infrared thermography," *IEEE Trans. Antennas Propag.*, vol. 70, no. 5, pp. 3799-3805, May 2022, doi: 10.1109/TAP.2021.3137491.

[16] M. Ziane, R. Sauleau, and M. Zhadobov, "Antenna/body coupling in the near-field at 60 GHz: Impact on the absorbed power density," *Appl. Sci.*, vol. 10, no. 21, p. 7392, Oct. 2020, doi: 10.3390/app10217392.

[17] M. Ziane, M. Zhadobov, and R. Sauleau, "High-resolution technique for near-field power density measurement accounting for antenna/body coupling at millimeter waves," *IEEE Antennas Wirel. Propag. Lett.*, vol. 20, no. 11, pp. 2151-2155, Nov. 2021, doi: 10.1109/LAWP.2021.3087019.

[18] M. Ziane, M. Zhadobov, R. Sauleau, "Exposure assessments in the near-field accounting for antenna/body interactions at millimeter waves: Absorbed power density reconstruction from E-field vector," in *BioEM 2022*, Nagoya, Japan, Jun. 19-24, 2022.

[19] A. R. Guraliuc, M. Zhadobov, O. De Sagazan, and R. Sauleau, "Solid phantom for body-centric propagation measurements at 60 GHz," *IEEE Trans. Microw. Theory Tech.*, vol. 62, no. 6, pp. 1373-1380, Jun. 2014, doi: 10.1109/TMTT.2014.2320691.

[20] S. Gabriel, R. W. Lau, and C. Gabriel, "The dielectric properties of biological tissues: II. Measurements in the frequency range 10 Hz to 20 GHz," *Phys. Med. Biol.*, vol. 41, no. 11, Nov. 1996, doi: 10.1088/0031-9155/41/11/002.

[21] D. W. Hahn, *Heat Conduction*, 3rd ed. Hoboken, N.J, USA: Wiley, 2012.

[22] J. P. Holman, *Experimental Methods for Engineers*, 8th ed. Boston, MA, USA: McGraw-Hill, 2012.

[23] International Commission on Non-Ionizing Radiation Protection (ICNIRP), "Guidelines for limiting exposure to electromagnetic fields (100 kHz to 300 GHz)," *Health Phys*., vol. 118, no. 5, pp. 483-524, May 2020, doi: 10.1097/HP.0000000000001210.